Supplementary Information

A. De,[1,*] P. Cook,[2,3,†] K. Collins,[1] W. Morong[‡],[1] D. Paz,[2] P. Titum,[1,4]
G. Pagano,[5] A. V. Gorshkov,[1] M. Maghrebi,[2] and C. Monroe[1,6,7]

[1]*Joint Quantum Institute and Joint Center for Quantum Information and Computer Science, NIST/University of Maryland, College Park, Maryland 20742*
[2]*Department of Physics and Astronomy, Michigan State University, East Lansing, Michigan 48824*
[3]*Facility for Rare Isotope Beams, East Lansing, Michigan 48824*
[4]*Johns Hopkins University Applied Physics Laboratory, Laurel, Maryland 20723*
[5]*Department of Physics and Astronomy, Rice University, Houston, TX, USA*
[6]*Department of Electrical and Computer Engineering, Department of Physics, Duke Quantum Center, Duke University, Durham, North Carolina 27708, USA*
[7]*IonQ Inc., College Park, Maryland 20742, USA*

Contents

I. Dynamical Phase Diagram from Mean-Field Analysis 2

II. LMG model 3
A. Gaussian Fluctuations 4
B. Critical Finite-Size Scaling 4
C. Finite-Size Behavior of the Order Parameter 6
D. Double (Multiple) Quenches 7

III. Power-law Interacting Spin Chain 9
A. Power-Law J_{ij} with Periodic Boundary Conditions 10
B. Power-Law J_{ij} with Open Boundary Conditions 11

IV. Long-range Interacting Spin Chain with Experimental J_{ij} 12

V. Experiment vs Theory 13
A. Finite-Size Behavior of the Order Parameter 13
B. Long-Range Character of J_{ij} Matrix 14
C. Correlation Matrix 14
D. Double Quench Switch Times 15

VI. Optimal Collapse Algorithm 16
A. Uncertainty Estimates via the Hessian 17

References 18

This document provides details of the theoretical analysis (sections I to IV), elaborates on and contrasts against the experimental results (section V), and finally provides the numerical approach used to determine the critical exponents and their errors (section VI).

‡ current address: AWS Center for Quantum Computing, Pasadena, California 91125, USA. Work done prior to joining AWS.
*Electronic address: arinjoy@umd.edu
†Electronic address: cookpat4@msu.edu

Theoretical Models

In this Supplemental Information, we consider theoretical models with a generalized long-range interaction:

$$H = -\frac{1}{2\mathcal{J}} \sum_{i \neq j}^{N} J_{ij} \left(\gamma^x \sigma_i^x \sigma_j^x + \gamma^y \sigma_i^y \sigma_j^y \right) + B \sum_{i}^{N} \sigma_i^z, \tag{1}$$

where σ_i^α with $\alpha = x, y, z$ are the usual Pauli operators for spin i, and

$$\mathcal{J} = \frac{1}{N-1} \sum_{i \neq j}^{N} J_{ij}, \tag{2}$$

is a normalization constant known as the Kac factor (or, Kac normalization). This normalization factor is particularly useful for long-range coupling as it renders the Hamiltonian extensive.

1. In section I, we provide a mean-field analysis to determine the dynamical phase diagram. We then consider three versions of the model described by eq. (1) ranging from the most idealized theoretical model to one that is most experimentally relevant.

2. In section II, we consider the collective Lipkin-Meshkov-Glick (LMG) model where $J_{ij} = 1$ and the interaction is infinite ranged. We provide a detailed analysis of the ground-state, the dynamical phase diagram as well as the critical properties. While an idealized model, it explains the main features of the experimental results.

3. In section III, we add another layer of complexity by considering a power-law interaction $J_{ij} \sim 1/|i-j|^p$ with open and periodic conditions. We show that, for $0 < p < 1$, this model exhibits the same dynamical phase diagram and critical properties.

4. Finally, in section IV, we theoretically analyze the long-range spin model with the experimental values of J_{ij}. The latter values fall off exponentially at large distances (see section V B), hence departing from the collective or the truly long-range variant of the previous models. Nonetheless, we show that the critical properties of the experimental model are consistent with those of the LMG model and its long-range variants.

Before continuing, we note that the experimental model is antiferromagnetic while the theoretical models considered here are ferromagnetic; however, we use a simple trick to relate the two models [1–3]. Given that the Hamiltonian is purely real (using the standard representation of Pauli matrices) and the fact that the correlation function $\langle \sigma_i^x \sigma_j^x \rangle$ is real, we have

$$\langle \sigma_i^x \sigma_j^x \rangle_{H,\psi_0,t} = (\langle \sigma_i^x \sigma_j^x \rangle_{H,\psi_0,t})^* = \langle \sigma_i^x \sigma_j^x \rangle_{-H,\psi_0,t}, \tag{3}$$

where we have made explicit the dependence on the Hamiltonian H, time t and the initial state ψ_0. We have furthermore assumed that the initial state is also real; for example, a fully polarized state along the negative z direction is real. By flipping the overall sign of the Hamiltonian, the antiferromagnetic coupling is then mapped to a ferromagnetic one.

I. Dynamical Phase Diagram from Mean-Field Analysis

In this section, we obtain the dynamical phase diagram using a mean-field analysis for the generalized model in eq. (1). Starting from the initial state $|\downarrow\downarrow \cdots\rangle$, we suddenly turn on an Ising-type Hamiltonian by setting $\gamma^x = 1$ and $\gamma^y = 0$. In a mean-field analysis, the Hamiltonian becomes

$$H = -m\sigma^x + B\sigma^z = \sqrt{m^2 + B^2}\ \mathbf{n} \cdot \boldsymbol{\sigma}, \tag{4}$$

where $m \equiv \langle \sigma^x \rangle$. We have dropped the site index, and defined the unit vector $\mathbf{n} = (n_x, 0, n_z)$ parallel to $(-m, 0, B)$. At long times after the sudden quench, the initial state dephases in the new basis defined by the operator $\mathbf{n} \cdot \boldsymbol{\sigma}$, and the time-averaged density matrix becomes

$$\lim_{t\to\infty} |\psi\rangle_t\langle\psi| = \sin^2\frac{\theta}{2}|\mathbf{n},+\rangle\langle\mathbf{n},+| + \cos^2\frac{\theta}{2}|\mathbf{n},-\rangle\langle\mathbf{n},-|, \tag{5}$$

where $\mathbf{n}\cdot\mathbf{z} = \cos\theta$. Using the identity $m = \langle\sigma^x\rangle$, we then find the self-consistent equation

$$m = -\cos\theta\sin\theta = \frac{m}{\sqrt{m^2+B^2}}\frac{B}{\sqrt{m^2+B^2}}, \tag{6}$$

which in turn yields the time-averaged order parameter as

$$m = \sqrt{B\,(1-B)}. \tag{7}$$

Furthermore, this equation predicts a dynamical phase transition at $B_c = 1$. This mean-field analysis is exact for the infinite-range LMG model. Furthermore, with the aid of spin-wave analysis, we show that it is also exact for the long-range model with $0 < p < 1$ (see section III), and additionally provides an excellent estimate for the phase transition corresponding to the experimental J_{ij} (see section IV).

II. LMG model

The LMG model is characterized by the infinite-range interaction with $J_{ij} \equiv 1$. This model can be reformulated in terms of total spin operators, with the Hamiltonian (up to a constant)

$$H_{LMG} = -\frac{2}{N}\left(\gamma^x S_x^2 + \gamma^y S_y^2\right) + 2BS_z, \tag{8}$$

where $S_\alpha = \frac{1}{2}\sum_i \sigma_i^\alpha$. At zero temperature, this model exhibits a quantum phase transition at $B_{gs,c} = 1$ [4]. Interestingly, the ground state critical point coincides exactly with the dynamical critical point obtained in the previous section. However, there are important distinctions: the order parameter's dependence on B is different. In fact, the ground state is perfectly ordered at $B = 0$ while the corresponding order parameter long after the sudden quench vanishes when $B = 0$. More importantly, the critical behaviour at the respective phase transitions is different: while the ground state exhibits a quantum phase transition at $B = 1$, the dynamical critical point shows distinct (and, effectively thermal) critical behaviour (see section II B). Furthermore, we show that for a double quench, the critical behaviour is neither quantum nor thermal, and is genuinely non-equilibrium (see section II D).

Beyond Mean Field

Next, we consider fluctuations at the phase transition. While the mean field solution in eq. (7) exactly describes the ordered phase (where $B < B_c = 1$) in the thermodynamic limit, fluctuations and finite-size scaling become important at or near the critical point for a finite system. To characterize fluctuations in the disordered phase as well as critical fluctuations near the critical point, one can use the Holstein-Primakoff transformation to map the spin operators of the LMG model to bosonic creation and annihilation operators as ($S_\pm = S_x \pm iS_y$)

$$S_- = S_+^\dagger = \sqrt{N - a^\dagger a}\,a \qquad S_z = -N/2 + a^\dagger a. \tag{9}$$

To the lowest order in $1/N$, we can identify

$$S_x \approx \sqrt{\frac{N}{2}}x, \qquad S_y \approx \sqrt{\frac{N}{2}}p. \tag{10}$$

Assuming that $\gamma^x > \gamma^y$, the dominant Ising interaction is along the x direction. In this case, the LMG Hamiltonian can be simply written as that of a harmonic oscillator [5],

$$H = \frac{1}{2m}p^2 + \frac{1}{2}m\Omega^2 x^2 + \frac{1}{4N}ux^4 + \cdots , \tag{11}$$

where we have defined $m^{-1} = 2\,(B-\gamma^y)$, $\Omega^2 = 4\,(B-\gamma^x)\,(B-\gamma^y)$, and $u = 2\gamma^x$. The dots in the above equation represent higher-order terms in $1/N$ or higher powers of x and p which are irrelevant at or away from the critical point in the disordered phase.

A. Gaussian Fluctuations

We begin by considering eq. (11) at the quadratic level in the disordered phase, before taking into account the interaction term ($\propto 1/N$). We are interested in the dynamics upon the sudden quench $(\gamma_0^{x,y}, B_0) \to (\gamma^{x,y}, B)$. Equivalently, we can consider a quench $(m_0, \Omega_0) \longrightarrow (m, \Omega)$ of the harmonic oscillator, where it is easy to solve for the time-averaged fluctuations:

$$\frac{1}{N}\overline{\langle S_x^2\rangle} = \frac{1}{2}\overline{\langle x^2\rangle} = \frac{m_0\Omega_0}{8m^2\Omega^2}\left(1 + \frac{m^2\Omega^2}{m_0\Omega_0^2}\right) , \tag{12}$$

where the overline indicates time averaging. Notice that fluctuations diverge where $\Omega = 0$, which in turn sets $(B-\gamma^x)(B-\gamma^y) = 0$. This condition coincides with the mean-field prediction in eq. (7) when $\gamma^x = 1$ and $\gamma^y = 0$; this is expected as the LMG model is infinite ranged. Furthermore, we can characterize the critical fluctuations beyond the mean-field prediction. We first observe that fluctuations scale as $\overline{\langle x^2\rangle} \sim 1/\Omega^2$ near the critical point. Comparing against the expression for a harmonic oscillator at high temperatures

$$\frac{1}{2}m\Omega^2\left\langle x^2\right\rangle \overset{T\gg\Omega}{\approx} \frac{1}{2}T,$$

we can identify an *effective temperature* [5]

$$T_{\text{eff}} = \frac{m_0\Omega_0}{4m} = \frac{B}{2}\sqrt{\frac{B_0-\gamma_0^x}{B_0-\gamma_0^y}}. \tag{13}$$

Specifically, in a quench starting from a product state corresponding to the ground state in the absence of the Ising interaction ($\gamma_0^{x,y} = 0$) to the critical point of the infinite-range Ising Hamiltonian ($\gamma^x = 1$, $\gamma^y = 0$, and $B = 1$), we find a constant effective temperature, $T_{\text{eff}} = 1/2$. We stress that such notion of the effective temperature does not mean that the system is in equilibrium; rather, it means that low-frequency modes (or, more precisely, the soft modes) have become effectively thermal. Indeed, one finds thermal critical behaviour and scaling in this type of quench [5]; see also fig. S1.

B. Critical Finite-Size Scaling

Fluctuations diverge as we approach the critical point $B \to 1$ either in the ground state or in a quench to the critical point. In a finite-size system, the fluctuations do not strictly diverge but rather scale with N in a nontrivial fashion:

$$\frac{1}{N}\langle S_x^2\rangle \sim N^{\alpha}. \tag{14}$$

Notice that in the disordered phase, we have $\alpha = 0$ indicating noncritical fluctuations while in the ordered phases $\alpha = 1$ due to ordering $\langle S_x\rangle \sim N$. Only at the critical point, α becomes a nontrivial critical exponent. For the quantum phase transition in the ground state, this exponent becomes $\alpha = 1/3$; see fig. S1(a). This should be contrasted with a thermal phase transition where this exponent becomes $\alpha = 1/2$. In a quench to the critical point, the system evolves and approaches a stationary state that is not an equilibrium state; however, the critical exponent takes the same value $\alpha = 1/2$ as thermal equilibrium; see fig. S1(b). One can view this as a consequence of the fact that the effective

temperature takes a finite nonzero value (see eq. (13)). Here, we derive this critical scaling using a simple analysis. Our approach is based on a non-equilibrium field theory which systematically leads to a semiclassical analysis similar to the truncated Wigner approximation (see Ref. [5] for more details). To this end, we start from the partition function

$$Z = \int Dx_{\pm} W_0 e^{i(S[x_+]-S[x_-])}\,, \tag{15}$$

where W_0 is the Wigner function corresponding to the initial state, and $[x_\pm(t)]$ denote forward and backward trajectories, respectively. These trajectories are weighted by the phase factors $\exp(\pm iS)$ where $S = \frac{1}{2}\int dt[m\dot{x}^2 - m\Omega^2 x^2 - (u/2N)x^4]$ is the corresponding action. Introducing the (Keldysh) variables $x_{c/q} = (x_+ \pm x_-)/\sqrt{2}$, the total (Keldysh) action becomes

$$S_K = S[x_+] - S[x_-] = -\int dt[m x_q \ddot{x}_c + r x_q x_c + (u/2N)(x_c^3 x_q + x_c x_q^3)]\,, \tag{16}$$

with $r = m\Omega^2$. We take the initial state as the ground state of the Hamiltonian in the absence of the Ising interaction. The Wigner function then becomes a Gaussian function of phase space variables as

$$W_0(x_0, p_0) \sim e^{-x_0^2 - p_0^2}\,. \tag{17}$$

Casting the Wigner function in terms of the configuration variables, the total partition function takes the form

$$Z = \int Dx_{c/q} e^{-x_{c0}^2/2l_0^2 - \dot{x}_{c0}^2/2v_0^2} e^{-\int dt[m x_q \ddot{x}_c + r x_q x_c + (u_c/2N)x_c^3 x_q + (u_q/2N)(x_c x_q^3)]}\,, \tag{18}$$

where we have introduced the parameters l_0 and v_0 for later convenience; for the coherent initial state assumed above, we have $l_0 = 1$ and $v_0 = 1/m_0$. We have also introduced the coefficients $u_{c/q}$ to distinguish the two interaction vertices; at the microscopic level, we have $u_c = u_q = u$. As pointed out in Ref. [5], to probe the behaviour at long times, we can rescale time $t \to t/\lambda$ and identify how various terms scale. We find that that under this rescaling $l_0 \to 0$ and $u_q \to 0$. The first condition imposes the boundary condition $x_{c0} = 0$ given the Gaussian distribution $\exp(-x_{c0}^2/2l_0^2)$. The latter condition simply means that the 'quantum' vertex proportional to u_q is less relevant than the classical vertex proportional to u_c, a condition that typically emerges in the semiclassical limit. Dropping the quantum vertex, we can integrate over the field x_q to find a delta function that imposes the semiclassical equation of motion together with a Gaussian distribution of the initial state (also changing the coordinate back to x via $x_c = \sqrt{2}x$ and restoring $u_c \to u$):

$$Z = \int Dx \delta(x_0) e^{-\dot{x}_0^2/v_0^2} \delta\left(m\ddot{x} + rx + \frac{u}{N}x^3\right)\,. \tag{19}$$

This equation admits a simple interpretation: A 'particle' whose position is given by x moves under a nonlinear equation of motion with the initial conditions where $x_0 = 0$ and $\dot{x}_0$ is drawn from a Gaussian distribution. This equation is simply the truncated Wigner approximation, which evolves the wavefunction with the classical equation of motion, but captures the (quantum) fluctuations of the initial state; the only difference is that, using a scaling argument, we have set $x_0 = 0$.

To characterize the critical behaviour, we can study the scaling behaviour of the above equation. We remark that, at the critical point $r = 0$, the partition function becomes scale invariant under the rescaling

$$t \to t/\lambda, \quad x \to x/\lambda, \quad N \to N/\lambda^4\,. \tag{20}$$

This immediately implies that fluctuations $\langle x^2 \rangle$ as a function of t and N both take the scaling form

$$\langle x(t)^2 \rangle = N^\alpha f(t/N^\zeta)\,, \tag{21}$$

with the critical exponents $\alpha = 1/2$ and the $\zeta = 1/4$; the latter exponent identifies a dynamical critical exponent. This is indeed consistent with the exact numerical calculation in fig. S1(b).

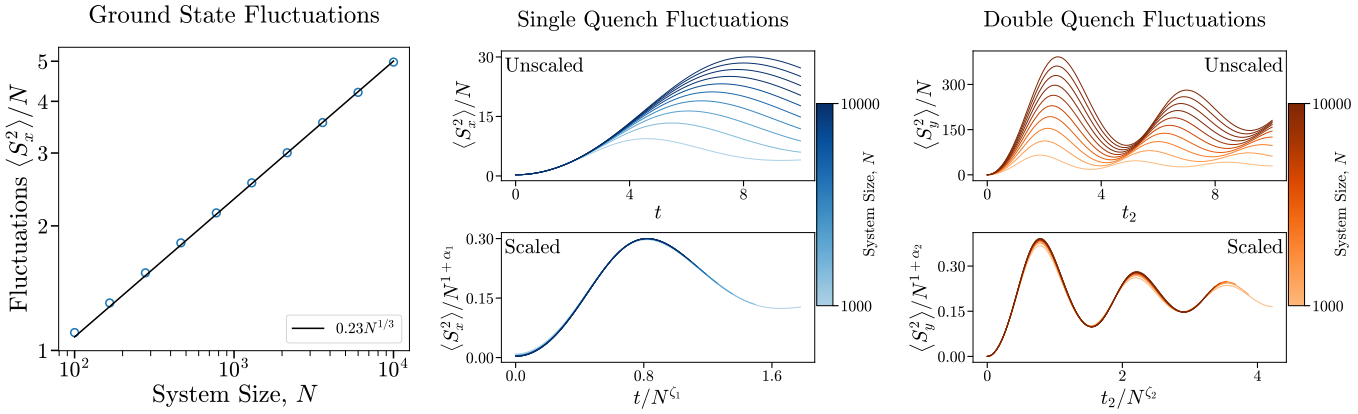

FIG. S1: Fluctuations scaling with system size at the critical point (a) in the ground state, (b) after a single quench, and (c) after a double quench. (b) A single quench from the disordered phase to the critical point $(B, \gamma^x, \gamma^y) = (1, 1, 0)$ gives rise the critical exponents $(\alpha_1, \zeta_1) = (1/2, 1/4)$. (c) A second quench to the other critical point $(B, \gamma^x, \gamma^y) = (1, 0, 1)$ is performed when the fluctuations in panel (b) reach their peak. The coordinate t_2 denotes the time since the second quench. The double quench gives rise to the critical exponents $(\alpha_2, \zeta_2) = (3/4, 1/8)$.

C. Finite-Size Behavior of the Order Parameter

In eq. (7), we have presented the mean-field prediction for the time-averaged order parameter in the ordered phase, $B < 1$, and in the thermodynamic limit $N \to \infty$. In the previous section, we have further investigated the critical fluctuations for finite system sizes *exactly* at the critical point $B = B_c = 1$. In this section, we study finite-size corrections in the *vicinity* of the critical point B_c. This is crucial to identify the dynamical phase transition in a finite-size system. To this end, we consider the equation of motion dictated by eq. (19):

$$\ddot{x} + rx + ux^3 = 0. \tag{22}$$

For notational convenience, we have set $m = 1$ and absorbed the factor proportional to $1/N$ into the definition of the interaction parameter u. For the purpose of this section, it suffices that

$$r \propto B - 1, \qquad u \propto 1/N\,. \tag{23}$$

In the quench starting from a disorded state, the initial conditions are set by $x(t = 0) = 0$ and $\dot{x}(0) = v$ where v is drawn from a Gaussian distribution $\exp(-Dv^2)$; the parameter D is set by the initial state, but we shall treat it as a phenomenological parameter. Solving the above equation with the initial conditions $x(t = 0) = 0$ and $\dot{x}(t = 0) = v$, we find

$$x_v(t) = \mathrm{sgn}(v)\,\mathrm{sn}\left(t\sqrt{\frac{r + \sqrt{r^2 + 2uv^2}}{2}}, \frac{r - \sqrt{r^2 + 2uv^2}}{r + \sqrt{r^2 + 2uv^2}}\right), \tag{24}$$

with $\mathrm{sn}(u, m)$ the Jacobi elliptic function. The above equation exhibits persistent oscillations. We are instead interested in the time average of $\overline{x(t)^2}$ which is given by

$$\overline{x_v^2} \equiv \lim_{t\to\infty} \overline{x_v(t)^2} = \frac{\sqrt{r^2 + 2uv^2} - r}{2u}\,. \tag{25}$$

Finally, the Gaussian integral over v (i.e., the integral $\langle\cdot\rangle_v \equiv \int dv \exp(-Dv^2) \cdot / \int dv \exp(-Dv^2)$) yields

$$\left\langle \overline{x_v^2} \right\rangle_v = -\frac{r}{2u} + \frac{U(-\frac{1}{2}, 0, Dr^2/(2u))}{\sqrt{2Du}}, \tag{26}$$

where U is Tricomi's confluent hypergeometric function. Making the dependence of u on N explicit by $u \to u/N$, we find

$$\overline{m^2} \equiv \frac{1}{N^2}\overline{\langle S_x(t)^2\rangle} = \frac{1}{N}\left\langle \overline{x_v^2} \right\rangle_v = -\frac{r}{2u} + \frac{1}{\sqrt{N}}\frac{U\left(-\frac{1}{2}, 0, DNr^2/(2u)\right)}{\sqrt{2Du}}. \tag{27}$$

Deep in the ordered phase, we must have $\overline{m^2} = m^2$ where the order parameter m is computed from mean field (see eq. (7)). This is indeed the case: the above equation captures the initial linear dependence of the order parameter on r as one enters the ordered phase, that is, $\overline{m^2} \sim |r| \propto (1-B)$ when $r < 0$, while the exact (mean-field) solution within the ordered phase is given by $m^2 = B(1-B)$. An expression that properly interpolates between the two extremes can be obtained by multiplying the right hand side of the above equation by a factor of B. We also fix the coefficient $u = 1/2$ to match eq. (7) deep in the ordered phase where $r < 0$. Making explicit the dependence on B and B_c, we find

$$\overline{m^2} = \frac{B}{B_c}\left[\left(1 - \frac{B}{B_c}\right) + \frac{1}{\sqrt{N}}\frac{U\left(-\frac{1}{2}, 0, DN(1-\frac{B}{B_c})^2\right)}{\sqrt{D}}\right]. \tag{28}$$

In a numerical calculation of the critical point, the above fit only contains two free parameters: the constant D and the critical point B_c.

In the experiment, it is more convenient to study the maximum of $\langle S_x^2\rangle/N^2$ in time rather than its stationary value. The above analysis remains valid but with an an overall amplitude, which we shall treat as a free parameter in eq. (28). In fig. S2, we show that that above function (up to an overall amplitude $\mathcal{A}$) is an excellent fit to the order parameter obtained from the exact numerical simulation, and the extracted value of the critical point is almost identical to the exact value of $B_c = 1$.

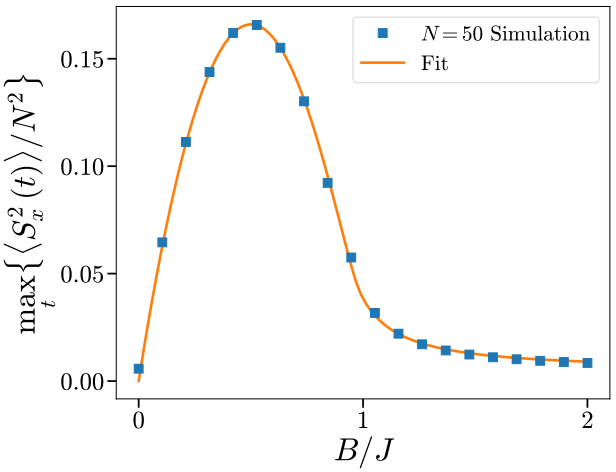

FIG. S2: The order parameter for the LMG model with $N = 50$ extracted from the peak of $\langle S_x^2(t)\rangle$. We also depict the fit function from eq. (28) with an overall factor $\mathcal{A} = 16.15(9)$, as well as the fit parameters $D = 0.34(1)$ and $B_c = 0.976(4)$ in excellent agreement with the exact critical point, $B_c = 1$.

D. Double (Multiple) Quenches

In this section, we analyze the scaling behaviour of the system as the result of a double quench starting from a disordered initial state to the critical point of the LMG model with $\gamma_0^x = 1$ and $\gamma_0^y = 0$, and, with a delay, a subsequent

quench to the critical point of the LMG model with $\gamma_0^x = 0$ and $\gamma_0^y = 1$; See Fig. 1(b) of the main text. Both critical points are defined by $B_c = 1$. Notice that the final Hamiltonian has the Ising interaction along the y direction only, and the dominant fluctuations correspond to the those along the y direction. To parallel the notation in the previous sections, we use the Holstein-Primakoff expansion but now identify, to the lowest order in $1/N$,

$$\sqrt{\frac{2}{N}} S_x \approx p_2 \,, \qquad \sqrt{\frac{2}{N}} S_y \approx x_2 \,, \tag{29}$$

as the dynamical variables upon a second quench, while we reserve x_1 and p_1 defined similarly to x and p in eq. (10), respectively, as the dynamical variables following the first but before the second quench. At the time of the second quench ($t_2 = 0$), we have $x_2 = p_1$ and $p_2 = x_1$ due to continuity. The Hamiltonian at each stage is given by $H_i = \frac{1}{2m_i} p_i^2 + \frac{1}{2} m_i \Omega_i^2 x_i^2$ where $i = 0, 1, 2$ correspond to pre-quench, first-quench, and second-quench variables; we also identify $x_0 = x_1$ and $p_0 = p_1$. To characterize fluctuations at the quadratic order, we shall consider a finite distance from the critical point at all stages of the dynamics (but approaching criticality when considering finite-size scaling). The frequencies Ω_i are then given by

$$\Omega_i^2 = 4 \left(B_i - J\gamma_i^x\right) \left(B_i - J\gamma_i^y\right) \tag{30}$$

and similarly for m_i; the exact values of m_i are unimportant and we just remark that they remain finite even as we approach the critical point.

Next, we characterize the dominant fluctuations ($\langle x_2^2 \rangle$) at late times from those of $\langle x_1^2 \rangle$ and $\langle p_1^2 \rangle$ long after the first quench but before the second quench. Finally taking the long-time average, we find

$$\overline{\langle x_2^2 \rangle} = \frac{\overline{\langle p_1^2 \rangle}}{2} + \frac{\overline{\langle x_1^2 \rangle}}{2 m_2^2 \Omega_2^2} = \frac{m_0^2 \Omega_0^2}{16} + \frac{m_1^2 \Omega_1^2}{16 m_0^2 \Omega_0^2} + \frac{1}{8 m_0 \Omega_0 m_2^2 \Omega_2^2} + \frac{m_0 \Omega_0}{8 m_1^2 \Omega_1^2 m_2^2 \Omega_2^2}. \tag{31}$$

where the frequencies Ω_i are defined above. For two successive quenches to the vicinity of critical points, $\Omega_2 \ll \Omega_1 \ll \Omega_0$, the above expression reduces to

$$\frac{1}{2} \overline{\langle x_2^2 \rangle} \sim \frac{m_0 \Omega_0}{16 m_1^2 \Omega_1^2 m_2^2 \Omega_2^2}. \tag{32}$$

Using the equipartition theorem $\frac{1}{2} m_2 \Omega_2^2 \langle x_2^2 \rangle \sim \frac{1}{2} T$, we can now identify an effective temperature upon the second quench (denoted by subscript 2) as

$$T_{\text{eff},2} = \frac{m_0 \Omega_0}{8 m_2 m_1^2 \Omega_1^2}. \tag{33}$$

Notice, however, that the effective temperature diverges as we tune the first quench to the critical point, $\Omega_1 \to 0$. Such divergence hints at a critical behaviour that is strongly athermal (see also Ref. [5]).

To characterize the critical behaviour, we can set up a scaling analysis using semiclassical dynamics. Using the continuity of these functions at $t_2 = 0$ where $x_2 = p_1$ and $\dot{x}_2 \sim p_2 = x_1$, the initial conditions for x_2 and its time derivative are given by a distribution function; we can alternatively characterize the same information via the expectation values

$$\langle x_2^2 \rangle \sim N^0, \quad \langle \dot{x}_2^2 \rangle \sim N^{\alpha_1}, \qquad \text{at } t_2 = 0 \,. \tag{34}$$

For a uniform notation, we have identified $\alpha_1 = \alpha$ as the critical exponent emerging in the first quench. To this end, a rather similar scaling analysis gives the partition function

$$Z = \int D x_2 \delta[x_2(0)] P\left[(\dot{x}_2(0))^2 / N^{\alpha_1}\right] \delta\left(m_2 \ddot{x}_2 + r_2 x_2 + \frac{u_2}{N} x_2^3\right) , \tag{35}$$

where $r_2 = m_2 \Omega_2^2$ and $u_2 = 2\gamma_2^y$; we have also defined $x_2(0) \equiv x_2(t_2 = 0)$ for ease of notation (similarly for $\dot{x}_2(0)$). To arrive at this equation, we have used the scaling limit where the quantum vertex can be ignored and the fluctuations

of x_2 right after the second quench ($t_2 = 0$) becomes a delta function. On the other hand, we keep track of the initial fluctuations of $\dot{x}_2$ and its scaling with system size N via the the distribution function P; for our purposes, only the scaling behaviour, and not the exact form of the function P, is important. We stress that the scaling variable in the argument of the function P is dictated by scaling behaviour in eq. (34) at the onset of the second quench.

Next, we observe that the partition function is scale-invariant (at $r_2 = 0$) upon the transformation

$$t \to t/\lambda, \quad x \to x/\lambda^{\frac{1+\alpha_1}{1-\alpha_1}}, \quad N \to N/\lambda^{\frac{4}{1-\alpha_1}} . \tag{36}$$

We can then immediately write a scaling relation for fluctuations

$$\langle x_2(t_2)^2 \rangle = N^{\alpha_2} g(t_2/N^{\zeta_2}) , \tag{37}$$

with g a scaling function and the critical exponents identified as

$$\alpha_2 = \frac{1+\alpha_1}{2}, \qquad \zeta_2 = \frac{1-\alpha_1}{2} . \tag{38}$$

Using $\alpha_1 = 1/2$ in the first quench, we find $\alpha_2 = \frac{3}{4}$ and $\zeta_2 = \frac{1}{8}$. These predictions are in excellent agreement the exact numerical simulation shown in fig. S1(c).

At this point, we can also determine the scaling of the effective temperature. Note that eq. (35) remains scale-invariant even for nonzero r_2 upon scaling $r_2 \to \lambda^2 r_2$, which then determines the scaling behaviour of this variable as $r_2 \sim N^{-2\zeta_2}$. Now recalling the definition of the effective temperature $\frac{1}{2}\Omega_2^2 \overline{\langle x_2^2 \rangle} \sim \frac{1}{2} T_{\text{eff},2}$ together with the facts $r_2 \propto \Omega_2^2 \sim N^{-2\zeta_2}$ and $\langle x_2^2 \rangle \sim N^{\alpha_2}$, we find

$$T_{\text{eff},2} = N^{\alpha_2 - 2\zeta_2} . \tag{39}$$

The same relation holds for the first quench by changing all the subscripts to 1. While in the latter case, $\alpha_1 - 2\zeta_1 = 0$ indicating a constant effective temperature, for a double quench $\alpha_2 - 2\zeta_2 = 1/2$ highlighting a nontrivial scaling of the effective temperature and a genuinely nonthermal critical behaviour.

We also remark that more generally for $k+1$ consecutive critical quenches $\gamma^x \to \gamma^y \to \gamma^x \to \cdots$ (showing only the nonzero anisotropy parameter) starting from a disordered state, we find the non-equilibrium critical exponents:

$$\alpha_{k+1} = \frac{1+\alpha_k}{2}, \qquad \zeta_{k+1} = \frac{1-\alpha_k}{4} , \tag{40}$$

and the effective temperature scaling

$$T_{\text{eff},k} \sim N^{\alpha_k - 2\zeta_k} , \tag{41}$$

with $\alpha_0 = 0$. One can solve the above iterative equations to find the exponents

$$\alpha_k = 1 - 2^{-k}, \qquad \zeta_k = 2^{-k-1} . \tag{42}$$

The critical exponents for single and double quench are recovered by setting $k = 1$ and 2, respectively. We can also determine the critical scaling of the temperature from eq. (41) as

$$T_{\text{eff},k} \sim N^{1 - \frac{1}{2^{k-1}}} . \tag{43}$$

III. Power-law Interacting Spin Chain

In this section, we extend our analysis to include the long-range model in eq. (1) where the interaction J_{ij} falls off as a power-law with the distance, $J_{ij} \sim 1/|i-j|^p$. We show, using a spin-wave analysis, that the universal behaviour

discussed in the text is governed by a collective mode as long as $0 < p < 1$, hence the same universality class as the LMG model discussed in the previous section. Furthermore, we show that the critical point is consistent with the mean-field (or, the LMG model's) prediction, i.e., $B_c = 1$, in the thermodynamic limit.

We begin by applying the Holstein-Primakoff transformation to eq. (1) at the level of individual spins

$$\sigma_i^- = (\sigma_i^+)^\dagger = \sqrt{1 - a_i^\dagger a_i} a_i \approx a_i, \qquad \sigma_i^z = 1 - 2a_i^\dagger a_i \,, \tag{44}$$

where we have neglected the non-linear terms. This approximation is valid as long as we remain in the disordered phase where the total spin is fully polarized along the z-direction, $\langle S_z \rangle = N/2$. Excitations of the bosonic degrees of freedom amount to fluctuations beyond this state. Under this approximation, the bosonic form of the Hamiltonian is given by

$$H = -\frac{1}{2\mathcal{J}} \sum_{ij} J_{ij} (a_i + a_i^\dagger)(a_j + a_j^\dagger) + 2B \sum_i a_i^\dagger a_i \,, \tag{45}$$

where we have neglected an unimportant constant, and have only included the quadratic terms in the Hamiltonian. This Hamiltonian, being quadratic in the bosonic operators, can be diagonalized via a Bogoliubov transformation. The form of this transformation depends on the form of J_{ij}. We first consider power-law interactions with periodic boundary conditions where simple analytical expressions can be obtained, and then extend our results to open boundary conditions. In the next section, we apply the same analysis to the experimental interaction matrix and contrast the results against those with a purely power-law interaction.

A. Power-Law J_{ij} with Periodic Boundary Conditions

For illustrative purposes, we first consider the case where J_{ij} is described by a power-law subject to periodic boundary conditions:

$$J_{ij} = \frac{J}{r_{ij}^p}, \qquad \text{with} \quad r_{ij} = \min(|i-j|, N - |i-j|) \,, \tag{46}$$

and $J_{ij} = 0$ when $i = j$. We can bring the Hamiltonian into a convenient form by going to the Fourier basis,

$$a_j = \frac{1}{\sqrt{N}} \sum_k e^{ijk} a_k \,, \tag{47}$$

where $k = 2\pi n/N$, $n \in \{0, \ldots, N-1\}$. The Hamiltonian now becomes diagonal in k,

$$H = \sum_k \begin{pmatrix} a_k^\dagger \\ a_{-k} \end{pmatrix}^T \begin{pmatrix} -\frac{\tilde{J}_k}{2\mathcal{J}} + B & -\frac{\tilde{J}_k}{2\mathcal{J}} \\ -\frac{\tilde{J}_k}{2\mathcal{J}} & -\frac{\tilde{J}_k}{2\mathcal{J}} + B \end{pmatrix} \begin{pmatrix} a_k \\ a_{-k}^\dagger \end{pmatrix} , \tag{48}$$

but remains to be diagonalized in terms of the bosonic operators. Here, we have defined

$$\tilde{J}_k = \sum_{r=-(N-1)/2}^{(N-1)/2} J_r e^{-irk} = 2J \sum_{r=1}^{(N-1)/2} \frac{1}{r^p} \cos(rk) \,, \tag{49}$$

and assumed that N is odd for simplicity. Next, we employ the Bogoliubov transformation,

$$a_k = \cosh(\theta_k) b_k + \sinh(\theta_k) b_{-k}^\dagger \,, \tag{50}$$

where $\theta_k = \theta_{-k}$, and the coefficients have been chosen to ensure that the new operators b_k satisfy the bosonic commutation relation $[b_k, b_{k'}^\dagger] = \delta_{kk'}$. To determine θ_k, we demand that this transformation diagonalizes eq. (48) as $H = \sum_k \omega_k b_k^\dagger b_k$, which leads to the relation

$$\tanh(2\theta_k) = \frac{\tilde{J}_k/2\mathcal{J}}{B - \tilde{J}_k/2\mathcal{J}}\,, \tag{51}$$

determining θ_k, as well as the mode frequencies

$$\omega_k = \sqrt{B(B - \tilde{J}_k/\mathcal{J})}\,. \tag{52}$$

With $\tilde{J}_0/\mathcal{J} = (N-1)/N$, we have $\omega_0 = \sqrt{B(B-1)}$ in the thermodynamic $N \to \infty$ limit. Therefore, the collective mode corresponding to $k = 0$ becomes gapless (or, *softens*) at the phase transition, and should be identified as the soft mode of the phase transition. For $B < 1$, the dispersion becomes complex valued and the Holstein-Primakoff transformation is no longer valid. Most importantly, we find that all the other modes beside the $k = 0$ mode remain gapped for long-range interactions with $p < 1$. This is because $\tilde{J}_k/\mathcal{J} < 1$ for any $k > 0$, therefore $\omega_k > 0$ at or away from the phase transition within the normal phase, $B \geq 1$. Indeed, one can show that the gap between the $k = 0$ mode and the next mode corresponding to $k = 2\pi/N$ remains finite for $p < 1$ even in the thermodynamic limit $N \to \infty$ [6]:

$$\lim_{N\to\infty} \omega_{k=2\pi/N} - \omega_{k=0} > 0, \tag{53}$$

at or beyond the critical point. This implies that the critical behaviour of long-range interactions with $p < 1$ is in the same universality class of the LMG model.

B. Power-Law J_{ij} with Open Boundary Conditions

It is generally expected that the bulk properties of a large system would be insensitive to boundary conditions at least for short-range interactions. The role of boundaries are, however, more pronounced in the presence of long-range interactions. Specifically, for truly long-range models with $p < 1$, the boundary conditions can even change the qualitative behaviour [7]. In this section, we show that open boundary conditions do not alter our conclusions for a long-range interacting chain with periodic boundary conditions. To perform a spin-wave analysis for J_{ij} (again taking $J_{ii} = 0$) without translation invariance, we cannot use the Fourier basis and instead carry out the Bogoliubov transformation directly in real space. We rewrite the Hamiltonian in the more convenient form

$$H = \sum_{i,j} \begin{pmatrix} a_i \\ a_i^\dagger \end{pmatrix}^\dagger \begin{pmatrix} A_{ij} & C_{ij} \\ C_{ij} & A_{ij} \end{pmatrix} \begin{pmatrix} a_j \\ a_j^\dagger \end{pmatrix}\,, \tag{54}$$

where $A_{ij} = -J_{ij}/2\mathcal{J} + B\delta_{ij}$, $C_{ij} = -J_{ij}/2\mathcal{J}$. Using the fact that the matrices $\mathbf{A}$ and $\mathbf{C}$ commute (the bold notation denotes matrix or vector objects), we can directly determine the Bogoliubov transformation which brings the above Hamiltonian into a diagonal form $H = \sum_k \Lambda_k b_k^\dagger b_k$ [8]. Specifically, the mode energies Λ_k are given by the square root of the eigenvalues of the matrix

$$\mathbf{M} = (\mathbf{A} + \mathbf{C})(\mathbf{A} - \mathbf{C}) = \mathbf{A}^2 - \mathbf{C}^2\,. \tag{55}$$

The eigenvalues can be determined numerically for an arbitrary interaction matrix J_{ij}.

In fig. S3, we consider J_{ij} matrix describing a power-law interacting chain with open boundary conditions and plot the mode frequencies Λ_0^2 and Λ_1^2 for $N = 50$ and $p = 0.9$; the value of p is chosen the mirror the experimental model although the latter features an exponential decay at large distances (see the next section). Λ_0 corresponds to the soft mode which, by definition, becomes gapless at the phase transition, $B \simeq 1$. (We recover $B_c = 1$ exactly in the thermodynamic limit.) In addition, we see that Λ_1 remains gapped even at the critical point, and therefore does not contribute the critical behaviour. Again, Λ_0^2 becomes negative for $B < 1$, and our bosonic mapping is no longer valid.

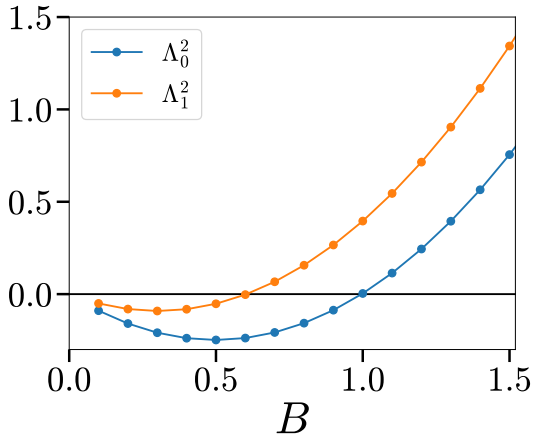

FIG. S3: The two lowest energy eigenvalues Λ_0 and Λ_1 corresponding to a power-law interaction with open boundary conditions, $p = .9$ for a system size of $N = 50$. While the lowest-frequency mode softens (i.e., $\Lambda_0 \to 0$) at the critical point, all the other modes remain gapped.

IV. Long-range Interacting Spin Chain with Experimental J_{ij}

In practice, the experimental values of the long-range coupling are not completely described by a power-law decay, and at large distances decay exponentially; see section V B. In spite of this, we show that, based on a spin-wave analysis, a phase transition still occurs close to the predicted critical point and that a single soft mode is responsible for the critical behaviour. To this end, we first note that the experimental Hamiltonian is given by eq. (1) without the Kac factor. In plotting various quantities however, we divide by the corresponding Kac factor to compare and contrast different cases on equal footing.

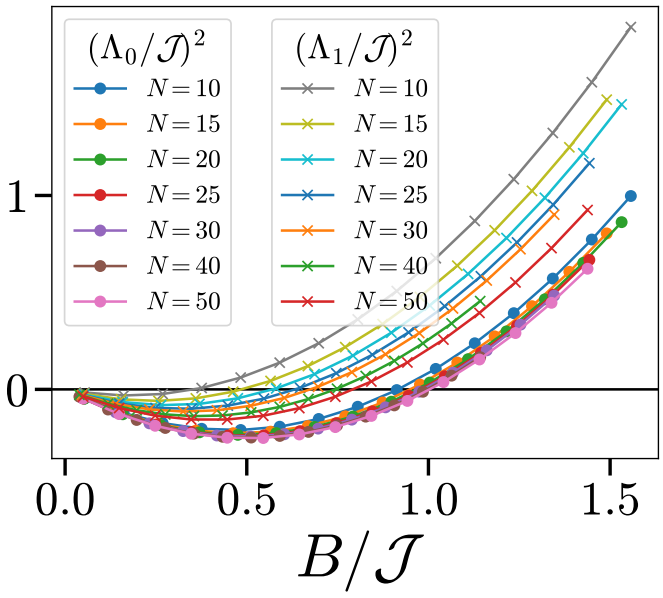

FIG. S4: The two lowest energy eigenvalues Λ_0 and Λ_1 versus the (Kac-normalized) transverse field $B/\mathcal{J}$, corresponding to the experimental J_{ij} for different system sizes; $\mathcal{J}$ is the Kac factor. The lowest-frequency mode softens, $\Lambda_0 \to 0$, approximately at the mean-field predicted critical point $B_c/\mathcal{J} = 1$. While the next eigenvalue Λ_1 becomes smaller for larger and larger system sizes, in contrast with a purely power-law J_{ij}, it remains finite even at the critical point (specifically, $\Lambda_1/\mathcal{J} \approx 0.5$ for $N = 50$ at $B = B_c$).

In fig. S4, we plot the first two lowest energy eigenvalues as a function of B for different system sizes each with

the corresponding experimental values of J_{ij}; we have divided B by the Kac factor $\mathcal{J}$ on the x-axis and re-scaled the eigenvalues accordingly. The points where the lowest-frequency mode softens (i.e., $\Lambda_0 \to 0$) agree very well with the mean-field prediction $B_c/\mathcal{J} \sim 1$. However, the gap between Λ_1 and Λ_0 (in units of the Kac factor) exhibits a strong dependence on system size, in contrast to the power-law case. This suggests a departure from the collective nature of the power-law interactions with $p < 1$ near the critical point. As Λ_1 becomes smaller, the corresponding mode becomes populated as well and contributes to the correlations. At the same time, we note that the latter mode still remains gapped even for $N = 50$ where $\Lambda_1/\mathcal{J} \sim 0.5$ at the critical point $B/\mathcal{J} \approx 1$ while $\Lambda_0 = 0$. Therefore, the soft mode corresponding to Λ_0 should govern the critical behaviour despite the model's departure from infinite- or truly long-range models considered before.

For a quantitative estimate of the contribution due to the first gapped mode (corresponding to Λ_1), let us first consider a toy model where a harmonic oscillator in its ground state undergoes a sudden frequency quench $\Omega_0 \to \Omega$. This quench excited the harmonic oscillator and creates a population of $n + 1/2 = \frac{1}{4}(\Omega/\Omega_0 + \Omega_0/\Omega)$. Now considering the first gapped mode, we can substitute $\Omega_0 = 2B$ and $\Omega = \Lambda_1$, which gives

$$n_1 \sim \frac{1}{2\Lambda_1/\mathcal{J}} \sim 1\,, \tag{56}$$

where the numerical estimate is computed by setting $B = B_c = \mathcal{J}$ and $\Lambda_1/\mathcal{J} \sim 0.5$ consistent with the data for $N = 50$ in fig. S4. This should be contrasted against the soft mode whose population scales with system size, according to our scaling analysis, as $n_0 \sim \sqrt{N}$ at the critical point. For $N = 50$, for example, this means that the soft mode is populated by $n_0 \lesssim 10$ in contrast with $n_1 \sim 1$. While the higher excited modes may be populated with $n \sim 1$, the soft mode still governs the critical behaviour at the phase transition.

V. Experiment vs Theory

In this section, we contrast various theoretical predictions against the experimental results.

A. Finite-Size Behavior of the Order Parameter

Mean-field analysis, together with finite-size corrections, yields eq. (28) up to an overall coefficient. Partial data and the comparison against the experiment is shown in Fig. 2(b) of the main text. In fig. S5, we provide additional information for larger system sizes and report the best fit for the critical point B_c.

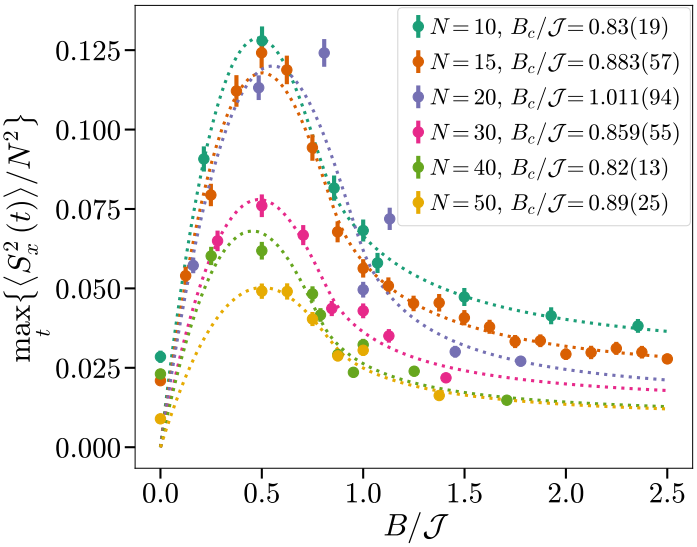

FIG. S5: Experimental data for the order parameter against the finite-size corrected mean-field prediction in eq. (28); $\mathcal{J}$ is the Kac normalization. The experimental data are well described by the theoretical finite-size correction.

We find that the experimental data are in good agreement with the mean-field prediction $B_c/\mathcal{J} = 1$.

B. Long-Range Character of J_{ij} Matrix

In fig. S6, we present the numerically calculated average interaction $J(r) = \frac{1}{N-r}\sum_i J_{i,i+r}$ as a function of distance r for $N = 10$, and 50. We first fit the numerical values to a pure power-law $J(r) \sim J(1)/r^p$ (dashed line in Fig. S6) and find the exponent p to be around 0.9 for both system sizes.

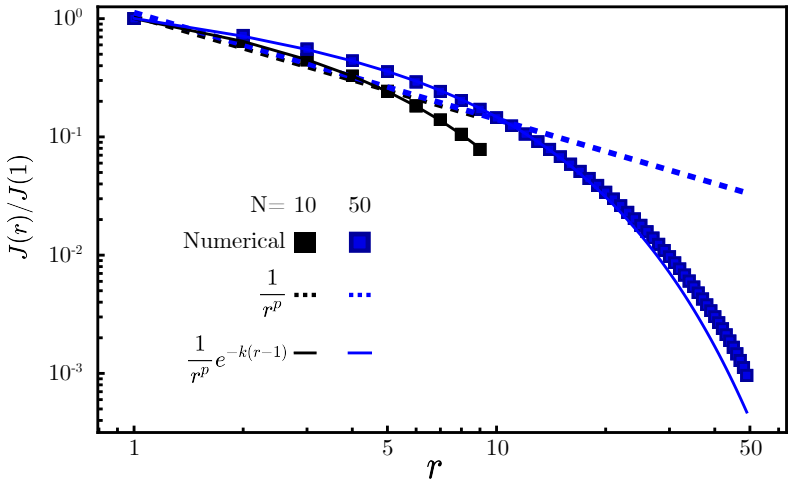

FIG. S6: Interaction profile $J(r)$ vs r. The numerical values of $J(r)$ are shown for system sizes $N = 10$, 50 (see the squares). A power-law fit, $J(r)/J(1) \sim r^{-p}$, gives $p = 0.89$ for both system sizes (see the dashed lines), and deviates from $J(r)$ at large distances. A better fit is provided by the product of a power-law with an exponential decay, $J(r)/J(1) \sim r^{-p}e^{-k(r-1)}$, and gives $p = 0.306$, $k = 0.231$ for $N = 10$, and $p = 0.306$, $k = 0.135$ for $N = 50$ (see the solid lines). The latter fit captures the trend of $J(r)$ at larger distances as well.

However, we note that the power-law fit deviates quite significantly from the calculated values, specifically at large distances and for larger system sizes. We further fit $J(r)$ against the product of a power-law and an exponentially decaying function of the form $J(r) = \frac{J(1)}{r^p}e^{-k(r-1)}$ [9]; see the solid lines in Fig. S6. We find the exponents $p = 0.306$, $k = 0.231$ for $N = 10$ and $p = 0.306$, $k = 0.135$ for $N = 50$ and note that the fit represents the numerical values closely. The similarity of the power-law exponents for two system sizes indicates that the experimental interaction matrices are self-similar at short distances. In section V C, we show that the spatial correlations after a single quench shows a slower decay compared to the spin-spin interactions. This behaviour is consistent with the critical correlations building up in the system.

C. Correlation Matrix

In this section, we provide the correlation matrix $\langle \sigma_i^x \sigma_j^x \rangle$ after a single quench. Specifically, we consider the average correlations between sites at a fixed distance r and at the same time as the peak of $\langle S_x^2 \rangle$, defined as $C(r) = \frac{1}{N-r}\sum_j \langle \sigma_j^x \sigma_{j+r}^x \rangle$. In fig. S7, we show the correlations in the experiment and contrast them against the exact simulation of the experimental model when available. Figure S7(a) shows that the correlation function is in reasonable agreement with the exact simulation. Sources of the remaining discrepancy are expected to include imperfect experimental detection and decoherence effects.

Figure S7(b) shows the correlation function for a system of size $N = 50$. Again, we find a much slower decay of the correlation function compared to the interaction profile $J(r)$, indicating criticality and long-range correlations in the system. On the other hand, the decay of the correlation function is relatively pronounced, a feature that should be contrasted against the LMG model (see section II) which shows no decay due to infinite-range interactions, and the purely power-law models (see section III) which are expected to show a relatively slow decay of the correlations with distance. This observation once again underscores the departure of the experiment from infinite- or truly long-range models with $p < 1$. In light of this, it is quite remarkable that the critical behaviour observed in the experiment is

almost identical to the latter models (cf. section IV).

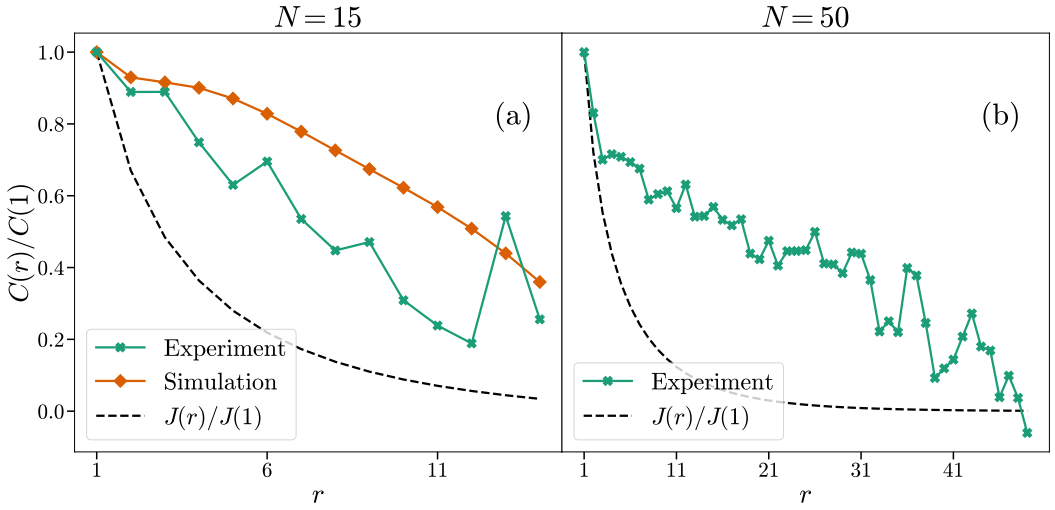

FIG. S7: Correlations upon a sudden quench to the critical point for (a) $N = 15$ and (b) $N = 50$; these correlations are measured/computed at the same time as the peak of $\langle S_x^2 \rangle$. (a) Correlations decay slowly compared to $J(r)$ indicating the build-up of critical fluctuations. (b) The data for $N = 50$ shows consistent results where correlations decay rather slowly compared to the interaction $J(r)$, indicating critical correlations. On the other hand, correlations decay significantly with r in contrast with the infinite- or truly long-range chain chains, reflecting the distinct character of the experimental system (see section V B).

D. Double Quench Switch Times

Our experimental and simulation data for the critical-to-critical quench does not collapse perfectly, even with exponents found by optimizing our objective function. We have found this to be primarily due to deviations in the time at which the second quench was performed in the experimental system, which were then used in the simulations.

The second quench should be performed at the same characteristic time for all system sizes; that is, the same critically scaled time of the first quench, $\mathcal{J}t/N^{\zeta_1}$ where $\zeta_1 \approx 1/4$. However, in order to avoid using the expected results in the data analysis, in Fig. 4 of the main text we restricted ourselves to choosing the switch time for each dataset (whether experiment or simulation) as the time at which the fluctuations in the experimental dataset were observed to reach a maximum, which has an inherent uncertainty due to the limited data sampling and experimental error sources. As a result, the switch times deviated around this value between system sizes.

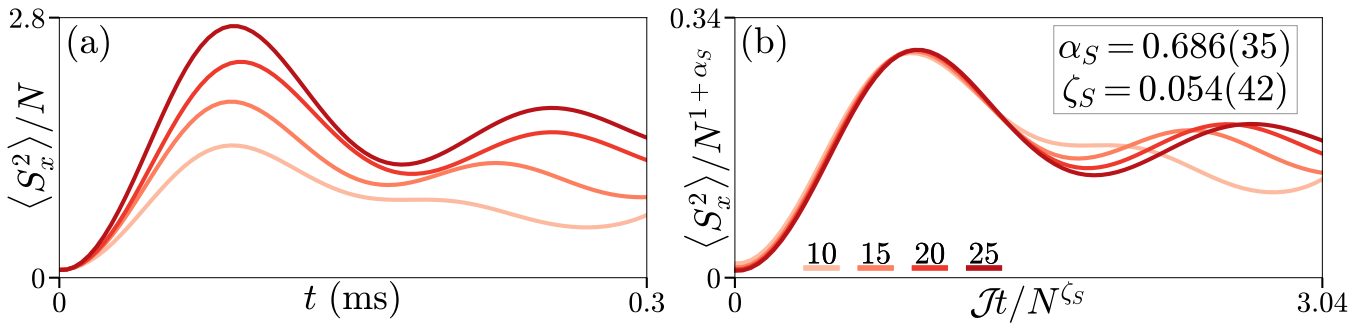

FIG. S8: Simulation of the experimental critical-to-critical quench using corrected switch times. These are to be compared to Fig. 4b,d of the main text, which instead use the best experimental estimates for these switch times. The critical exponents are calculated using the dynamics up to the first minimum after the first maximum, just as in the main text. The collapse up to and including the first peak is nearly perfect with the critical exponents that are in much better agreement with the theory prediction.

In fig. S8, we show results from simulating the experimental system with identical characteristic times. This figure demonstrates that, with the corrected quench times, the data collapse nearly exactly.

VI. Optimal Collapse Algorithm

To determine the scaled data shown in Figs 3c,d and 4c,d of the main text, we construct an objective function to measure the quality of the collapse of several curves each with some uncertainty. Previous work has used an objective function similar to the weighted-squared-difference, where all curves are linearly interpolated together to produce an estimate for the so-called "master-curve," from which the error is calculated as the distance to each curve [10]. Here we propose an alternative objective function that is more general and less sensitive to noise in the input data.

We define a curve in this context as a set of data points with associated uncertainties. Each point is denoted by $\mathbf{p} \equiv [x, y, \Delta x, \Delta y] \equiv [\mathbf{p}_x, \mathbf{p}_y, \Delta\mathbf{p}_x, \Delta\mathbf{p}_y]$, and a curve with k data points by $C \equiv \{\mathbf{p}\} \in \mathbb{R}^{4\times k}$. We first consider the case of two curves, C and C' with k and k' data points with k and k' not necessarily equal. We begin by equally normalizing the two curves in both x and y such that they are wholly contained within the region $[0,1]\times[0,1]$. Denote these normalized curves by $\overline{C}$ and $\overline{C'}$ given by

$$\begin{aligned}
Y_{\max} &= \max_{\mathbf{p}\in C\cup C'} \mathbf{p}_y, \qquad X_{\max} = \max_{\mathbf{p}\in C\cup C'} \mathbf{p}_x, \\
Y_{\min} &= \min_{\mathbf{p}\in C\cup C'} \mathbf{p}_y, \qquad X_{\min} = \min_{\mathbf{p}\in C\cup C'} \mathbf{p}_x, \\
\overline{C} &= \left\{ \frac{\mathbf{p} - X_{\min}}{X_{\max} - X_{\min}}, \frac{\mathbf{p}_y - Y_{\min}}{Y_{\max} - Y_{\min}}, \frac{\Delta\mathbf{p}_x}{X_{\max} - X_{\min}}, \frac{\Delta\mathbf{p}_y}{Y_{\max} - Y_{\min}} \middle| \mathbf{p} \in C \right\}, \\
\overline{C'} &= \left\{ \frac{\mathbf{p}' - X_{\min}}{X_{\max} - X_{\min}}, \frac{\mathbf{p}'_y - Y_{\min}}{Y_{\max} - Y_{\min}}, \frac{\Delta\mathbf{p}'_x}{X_{\max} - X_{\min}}, \frac{\Delta\mathbf{p}'_y}{Y_{\max} - Y_{\min}} \middle| \mathbf{p}' \in C' \right\}.
\end{aligned} \tag{57}$$

We define the loss function for a single point in $\overline{C}$ relative to $\overline{C'}$, $L\left(\mathbf{p}\in\overline{C}, \overline{C'}\right)$, using the square of the distance from the point to the nearest line segment in $\overline{C'}$, weighted by the square of the uncertainty in that distance. If the point in $\overline{C}$ falls outside of the bounds of $\overline{C'}$ then the loss is 0.

$$L\left(\mathbf{p}\in\overline{C}, \overline{C'}\right) = \begin{cases} 0 & \text{if } \mathbf{p}_x < \min_{\mathbf{p}'\in C'} \mathbf{p}'_x \text{ or } \mathbf{p}_x > \max_{\mathbf{p}'\in C'} \mathbf{p}'_x, \\ D^2\left(\mathbf{p}, \overline{C'}\right) / \Delta^2\left(\mathbf{p}, \overline{C'}\right) & \text{otherwise,} \end{cases} \tag{58}$$

where $D^2\left(\mathbf{p}, \overline{C'}\right)$ is the square of the distance from $\mathbf{p}$ to the nearest line segment in $\overline{C'}$,

$$\begin{aligned}
D^2\left(\mathbf{p}, \overline{C'}\right) &\equiv \frac{\left[\left(\mathbf{q}'_x - \mathbf{r}'_x\right)\left(\mathbf{r}'_y - \mathbf{p}_y\right) - \left(\mathbf{r}'_x - \mathbf{p}_x\right)\left(\mathbf{q}'_y - \mathbf{r}'_y\right)\right]^2}{\left(\mathbf{q}'_x - \mathbf{r}'_x\right)^2 + \left(\mathbf{q}'_y - \mathbf{r}'_y\right)^2}, \\
\mathbf{q}' &\equiv \underset{\substack{\mathbf{b}'\in\overline{C'} \\ \mathbf{b}'_x \geq \mathbf{p}_x}}{\operatorname{argmin}} \left|\mathbf{b}'_x - \mathbf{p}_x\right|, \\
\mathbf{r}' &\equiv \underset{\substack{\mathbf{b}'\in\overline{C'} \\ \mathbf{b}'_x \leq \mathbf{p}_x}}{\operatorname{argmin}} \left|\mathbf{b}'_x - \mathbf{p}_x\right|,
\end{aligned} \tag{59}$$

and $\Delta^2\left(\mathbf{p}, \overline{C'}\right)$ is the square of the uncertainty in that distance, found by propagating the uncertainties in the relevant parameters. Note that points which fall outside the domain of C' are given a loss of 0, since they have no corresponding line segment in C'. A diagram of this calculation is shown in fig. S9.

From this formulation it is clear that the loss of a point in $\mathbf{p}\in C$ that falls exactly on some part of C' is 0, and that if the uncertainty of C' in the region of $\mathbf{p}$ is large then the loss will be small.

We can then define the cost function between the two curves C and C', $s\left(C, C'\right)$ as the sum of the losses of each point in $\overline{C}$ relative to $\overline{C'}$, and vice versa, normalized by the number of points which were not excluded in eq. (58),

$$s\left(C, C'\right) \equiv \frac{1}{2}\left[\frac{\sum_{\mathbf{p}\in\overline{C}} L\left(\mathbf{p}, \overline{C'}\right)}{\left|\overline{C}\right|_{\overline{C'}}} + \frac{\sum_{\mathbf{p}'\in\overline{C'}} L\left(\mathbf{p}', \overline{C}\right)}{\left|\overline{C'}\right|_{\overline{C}}}\right], \tag{60}$$

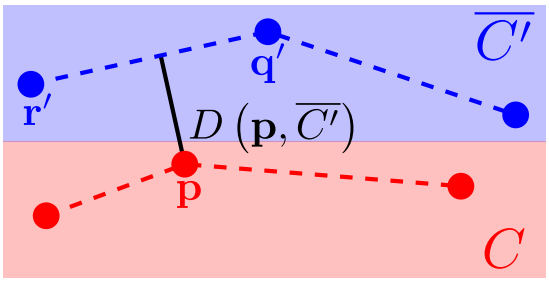

FIG. S9: Illustration of the calculations involved in the loss function, eq. (58).

where

$$|A|_B \equiv \sum_{\substack{\mathbf{a}\in A \\ \min_{\mathbf{b}\in B} \mathbf{b}_x \leq \mathbf{a}_x \leq \max_{\mathbf{b}\in B} \mathbf{b}_x}} \tag{61}$$

denotes the number of elements in A which fall within the domain of B.

Finally, the objective function for determining the collapse of a set of N curves $C_1, C_2, \ldots, C_N$ is

$$S(C_1, C_2, \ldots, C_N) \equiv \frac{1}{N^2 - N} \sum_{i<j}^{N} s\left(C_i, C_j\right). \tag{62}$$

The normalization of $N^2 - N$ arises from the number of pairs of non-identical curves in the set.

We perform convex optimization on this objective function with our data using Powell's method [11] in order to determine the critical exponents which result in an optimal collapse. Figure S10 shows the output space of our objective function, demonstrating that it is well-behaved and exhibits an identifiable minimum.

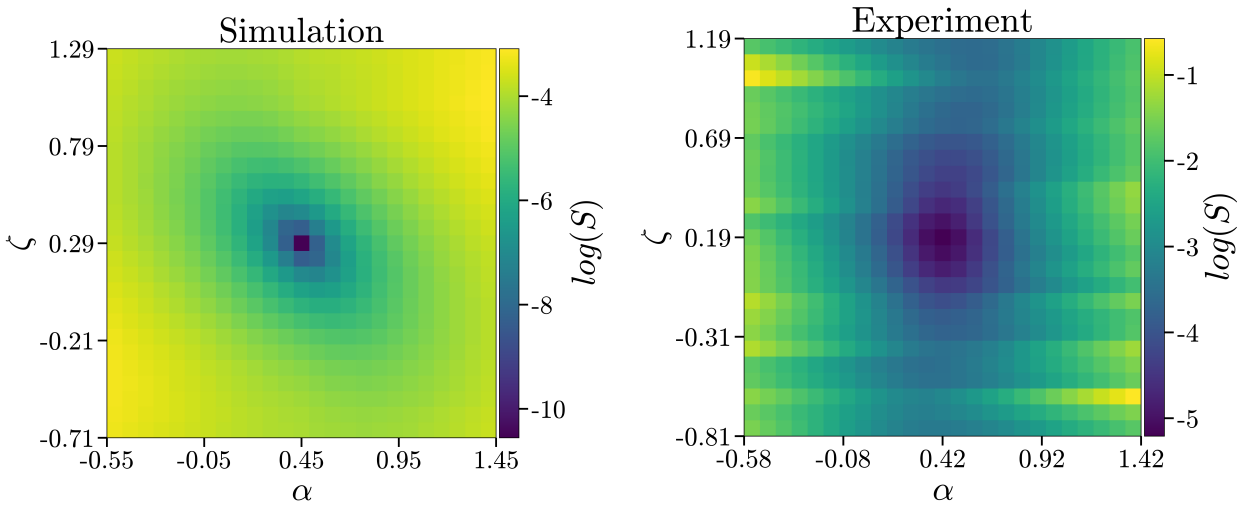

(a) (b)

FIG. S10: Output space of the objective function, eq. (62), around the calculated minimum for the (a) simulated and (b) experimental type-I quenches.

A. Uncertainty Estimates via the Hessian

Equation (62) incorporates the uncertainty in the data directly. To obtain an uncertainty in the predicted minimum location of the objective function, we use the Hessian. The uncertainty of any quantity X as a function of the input

parameters $\{x_i\}$ of an objective function f can be estimated by [12]

$$\Delta\left(X\right)^2 = \left(\tilde{f} - \hat{f}\right) \sum_{i,j} H_{ij}^{-1} \frac{\partial X}{\partial x_i} \frac{\partial X}{\partial x_j}. \tag{63}$$

Where H^{-1} is the inverse of the Hessian matrix of f evaluated at the location of the predicted minimum, $\tilde{f}$ is the value of f evaluated at the same location, and $\hat{f}$ is the true global minimum value of the objective function.

In our application $\{x_i\} = \{\alpha, \zeta\}$, and $X = \alpha$ or ζ as well. Moreover, we have designed our objective function such that the global minimum occurs when the curves perfectly collapse and so $\hat{f} = 0$. Therefore the uncertainty in the predicted exponents $\tilde{\alpha}$ and $\tilde{\zeta}$ is simply given by

$$\begin{aligned} \Delta\tilde{\alpha} &= \sqrt{S\left(\tilde{\alpha}, \tilde{\zeta}\right) H_{\alpha\alpha}^{-1}}, \\ \Delta\tilde{\zeta} &= \sqrt{S\left(\tilde{\alpha}, \tilde{\zeta}\right) H_{\zeta\zeta}^{-1}}. \end{aligned} \tag{64}$$

[1] Islam R., Senko C., Campbell W. C., Korenblit S., Smith J., Lee A., Edwards E. E., Wang C.-C. J., Freericks J. K., and Monroe C. Emergence and frustration of magnetism with variable-range interactions in a quantum simulator. *Science*, 340(6132):583–587, 2013.

[2] Jurcevic P., Shen H., Hauke P., Maier C., Brydges T., Hempel C., Lanyon B. P., Heyl M., Blatt R., and Roos C. F. Direct observation of dynamical quantum phase transitions in an interacting many-body system. *Phys. Rev. Lett.*, 119:080501, Aug 2017.

[3] Tan W. L., Becker P., Liu F., Pagano G., Collins K., De A., Feng L., Kaplan H., Kyprianidis A., Lundgren R., et al. Domain-wall confinement and dynamics in a quantum simulator. *Nature Physics*, 17(6):742–747, 2021.

[4] Suzuki S., Inoue J.-i., and Chakrabarti B. K. *Quantum Ising phases and transitions in transverse Ising models*, volume 862. Springer, 2012.

[5] Titum P. and Maghrebi M. F. Nonequilibrium criticality in quench dynamics of long-range spin models. *Phys. Rev. Lett.*, 125:040602, Jul 2020.

[6] Defenu N. Metastability and discrete spectrum of long-range systems. *Proceedings of the National Academy of Sciences*, 118(30):e2101785118, 2021.

[7] Hauke P. and Tagliacozzo L. Spread of correlations in long-range interacting quantum systems. *Phys. Rev. Lett.*, 111:207202, Nov 2013.

[8] Colpa J. H. P. Diagonalization of the quadratic boson hamiltonian. *Physica A: Statistical Mechanics and its Applications*, 93(3):327–353, September 1978.

[9] Pagano G., Bapat A., Becker P., Collins K. S., De A., Hess P. W., Kaplan H. B., Kyprianidis A., Tan W. L., Baldwin C., Brady L. T., Deshpande A., Liu F., Jordan S., Gorshkov A. V., and Monroe C. Quantum approximate optimization of the long-range Ising model with a trapped-ion quantum simulator. *PNAS*, **117**(41), (2020).

[10] Houdayer J. and Hartmann A. K. Low-temperature behavior of two-dimensional gaussian ising spin glasses. *Phys. Rev. B*, 70:014418, Jul 2004.

[11] Powell M. J. D. An efficient method for finding the minimum of a function of several variables without calculating derivatives. *The Computer Journal*, 7(2):155–162, 01 1964.

[12] Pumplin J., Stump D. R., and Tung W. K. Multivariate fitting and the error matrix in global analysis of data. *Phys. Rev. D*, 65:014011, Dec 2001.